Arch. Metall. Mater. **71** (2026), 1, 263-267

DOI: https://doi.org/10.24425/amm.2026.157787

PENGXIAN ZHANG[1*], J. YANG[1], YUANHANG XING[1]

DUAL-OBJECTIVE OPTIMIZATION OF PBF-LB PROCESS VIA ENERGY DENSITY CONTROL

This study introduces a dual-objective optimization framework for the laser powder bed fusion (PBF-LB) of TC11 titanium alloy, designed to concurrently mitigate deformation and improve densification. A multiphysics finite element model, which incorporates temperature-dependent material properties, was developed to investigate the deformation mechanisms across an energy density range of 21.2-54.5 J/mm^3. Experimental validation, conducted using 3D laser scanning, demonstrated close alignment with the predicted outcomes, with maximum deviations ranging from 0.04 to 0.08 mm. Systematic density measurements uncovered the nonlinear coupling effects between laser power and scan speed, resulting in an empirical power-velocity equation ($P = 0.2V + 30$, where P denotes laser power and V represents scanning speed), which yielded a peak relative density of 99.2%. The proposed strategy offers a comprehensive approach to the precision manufacturing of complex PBF-LB components, effectively balancing dimensional accuracy with mechanical performance, while minimizing experimental effort.

Keywords: Laser powder bed fusion; TC11 titanium alloy; Process parameter optimization; Deformation; Density

1. Introduction

Laser powder bed fusion (PBF-LB) is a near-net-shape additive manufacturing process widely adopted in the aerospace sector for producing high-performance titanium alloy components such as impellers and turbine blades. It offers short production cycles, high material utilisation, and the capability to fabricate complex geometries [1,2]. However, the nonlinear coupling of process parameters – laser power (P), scanning velocity (V), layer thickness (h), and hatch spacing (d) – creates dual challenges: controlling macroscopic deformation and achieving microstructural densification. Excessive energy input causes thermal stress accumulation (dimensional deviation >0.5 mm), while insufficient energy density results in unfused porosity (>5%) [3,4].

In addition to these parameters, scanning strategy [5], substrate preheating [6], atmosphere composition [7], and powder characteristics [8] also affect part quality. Although conventional optimisation approaches, such as orthogonal experiments [9,10] and response surface methodology [11,12], can reduce testing costs, they often fail to balance dimensional accuracy and mechanical performance, limiting PBF-LB applications in precision dynamic components [13].

Volumetric energy density ($E = P/(V \cdot h \cdot d)$) is frequently used as an integrated parameter for process optimisation and cross-study comparison [14,15]. However, studies have shown that even at constant E, variations in power and speed combinations significantly alter microstructure and properties in Ti-6Al-4V and Al-12Si alloys [16,17], indicating that E alone cannot reliably predict material performance.

To overcome these challenges, this study introduces a dual-objective optimisation framework for PBF-LB of TC11 titanium alloy impellers, featuring two core innovations: (1) quantitative assessment of energy density (21.2-54.5 J/mm^3) effects on impeller deformation via thermomechanical modelling, enabling accurate prediction; and (2) establishment of an empirical power-velocity relation ($P = 0.2V + 30$) for melt pool stabilisation, achieving 99.2% relative density in thin-walled regions (≤1 mm) and surpassing conventional E-based models.

2. Materials and methodology

2.1. Materials

The TC11 titanium alloy powder used in this study was supplied by Xi'an OZ Technology Co., Ltd. and produced via the plasma rotating electrode process (PREP) [18]. It is an $\alpha + \beta$ dual-phase titanium alloy with a nominal composition of

---

[1] SCHOOL OF MATERIALS SCIENCE AND ENGINEERING, LOUZHOU UNIVERSITY OF TECHNOLOGY, LANZHOU, 730070, P.R. CHINA

[*] Corresponding author: 13993195279@139.com

Ti–6.5Al–3.5Mo–1.5Zr–0.3Si (wt.%). The detailed chemical composition and particle size distribution data are provided in Tables S1 and S2 of the Supplementary Material. The morphology of the TC11 powder is shown in Figs. S1 to S3 of the Supplementary Material. The powder exhibited a particle size range suitable for laser powder bed fusion (PBF-LB), with characteristic particle diameters conforming to standard specifications for the process. Figs. S4 and S5 of the Supplementary Material show the experimental equipment and sample preparation platform, while Fig. S6 presents the final fabricated sample, the PBF-LB formed TC11 titanium alloy impeller.

2.2. Multiphysics modeling workflow

A comprehensive multiscale modeling framework was developed to simulate the macro–micro coupled behavior during the laser powder bed fusion (PBF-LB) of TC11 titanium alloy. Temperature-dependent thermophysical properties, spanning from 25°C to 1600°C (at 100°C intervals), were computed using JMatPro 11.0 [19], which has been validated for predicting thermal conductivity in titanium alloys with an error margin of less than 5% [20]. The obtained properties included thermal conductivity (5.8-24.6 W/m·K) [21], specific heat capacity (520-830 J/kg·K), and the coefficient of thermal expansion (9.2×10^{-6}-11.7×10^{-6}/°C), as shown in Fig. 1. The β-transus temperature was calculated to be 998°C through thermodynamic analysis, and the latent heat of phase transformation (419 kJ/kg) was incorporated for subsequent thermal stress analysis.

The computed parameters were integrated into the Simufact Additive 2022 material database to develop a TC11-specific material model. The impeller geometry was discretized using a voxel-based mesh (voxel size = 1 mm; refer to Fig. 2), resulting in approximately 2.1×10^6 hexahedral elements. The volumetric energy density is defined as:

$$E = \frac{P}{V * d * h} \tag{1}$$

Where E represents the energy density (J/mm^3), P denotes the laser power (W), V is the scan speed (mm/s), d is the hatch spacing (mm), and h is the layer thickness (mm). The hatch spacing and layer thickness were fixed at 0.11 mm and 0.06 mm, respectively, ensuring consistency in the experimental setup. The laser spot diameter was set between 70 and 100 µm, and the substrate preheating temperature was maintained at 80°C. A Python automation script was employed to generate parameter sets spanning energy density levels from 21.2 to 54.5 J/mm^3, requiring a total computational time of 187 hours.

2.3. Experimental design

A two-stage experimental protocol was developed to validate the multiphysics model within the dual-objective optimization framework. Stage 1: Energy Density-Deformation Mapping. This stage aimed to establish a quantitative relationship between volumetric energy density and the resulting deformation. Six energy density levels (21.2-54.5 J/mm^3) were systematically generated by varying laser power (210-360 W) and scan speed (1000-1500 mm/s), while layer thickness (h = 0.06 mm) and hatch spacing (d = 0.11 mm) were kept constant (see TABLE 1). Each parameter set was tested in triplicate to ensure statistical reliability and consistency. After printing, supports were removed via wire EDM, and full-field deformation measurements were captured using 3D laser scanning (Keyence VR-3200, accuracy ±5 µm) across critical regions, including blade tips and

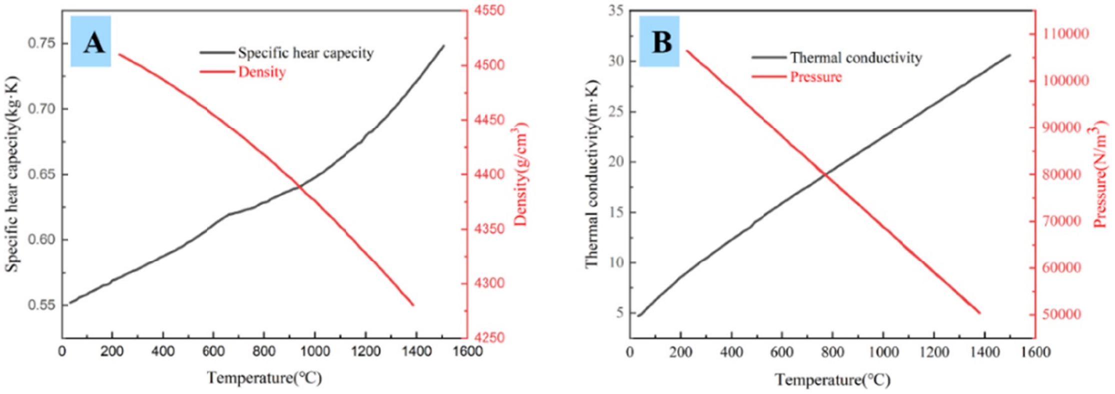

Fig. 1. JMatPro Thermophysical Properties of Titanium Alloy TC11: A – Density and Specific Heat Capacity vs. Temperature Curves; B – Thermal Conductivity and Young's Modulus vs. Temperature Curves

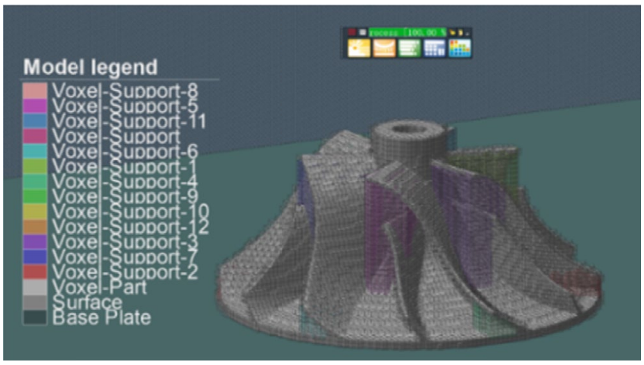

Fig. 2. Simufact model Voxel delineation map

overhangs. The relative error between simulated and measured dimensions was calculated as:

$$\theta = \pm \frac{N - M}{N} \times 100\% \tag{2}$$

where M denotes the mean measured dimension and N the nominal dimension.

Stage 2: Densification-Oriented Optimization. This stage was focused exclusively on maximizing relative density through a structured parameter optimization approach. A full factorial design was employed, featuring six levels of laser power (210-360 W) and scan speed (1000-1600 mm/s), resulting in 36 distinct parameter combinations (TABLE 2). Cubic specimens ($15 \times 15 \times 10$ mm^3) were fabricated in randomized positions on the build platform to minimize any bias resulting from localized thermal history. Density was measured using Archimedes' principle (ASTM B962), with five replicates per parameter set to ensure statistical robustness.

Validation trials on critical parameters (P = 300 W, V = 1200 mm/s, E = 37.88 J/mm^3) were conducted using ANOVA ($\alpha = 0.05$) to confirm statistical consistency between simulated and experimental data, with error bands defined by the 3σ criterion (99.7% confidence).

TABLE 1

Experimental process parameters

Experiment number	Laser power (W)	Scanning speed (mm/s)	Energy density (J/mm^3)
1	210	1500	21.212
2	240	1400	25.974
3	270	1300	31.469
4	300	1200	37.879
5	330	1100	45.455
6	360	1000	54.545

TABLE 2

Optimized parameters for PBF-LB forming process
of TC11 titanium alloy

Process parameters	Parameters
Laser power P (W)	250, 270, 290, 310, 330, 350
Scanning speeds V (mm/s)	1100, 1200, 1300, 1400, 1500, 1600
Powder thickness h (mm)	0.02, 0.04, 0.06
Scanning distance d (mm)	0.09, 0.11, 0.13

3. Results and validation

3.1. Validation of energy density-deformation relationship

Energy density gradient experiments revealed nonlinear deformation evolution in TC11 impellers (Fig. 3). When energy density increased from 21.2 J/mm^3 to 54.5 J/mm^3, the maximum tip deformation ($\delta_{\max}$) escalated from 0.29 mm to 0.73 mm, following the exponential model:

$$\delta_{\max} = 0.021 e^{0.038E} \ (R^2 = 0.983)$$

3D laser scanning validation (Fig. 4) demonstrated a root mean square error (RMSE) of 0.059 mm between simulated and experimental data. The maximum absolute deviation occurred at E = 25.9 J/mm^3 (Δ = 0.08 mm), corresponding to a relative error of 26.7%.

ANOVA analysis ($\alpha = 0.05$, $F = 2.34$, $p = 0.12$) confirmed no statistically significant difference between simulated and experimental data, with all error points residing within the 3σ confidence bands (±0.129 mm), thereby validating the model reliability.

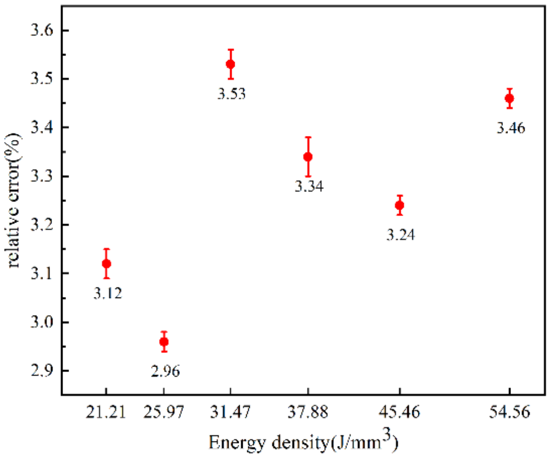

Fig. 3. Relative blade error for each energy density

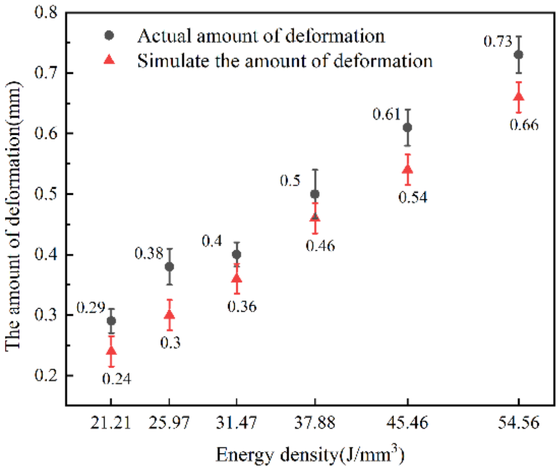

Fig. 4. Plot of energy density versus maximum simulated and actual deformations

3.2. Mechanism of process parameters on densification

The influence of process parameters on the relative density of TC11 titanium alloy during laser powder bed fusion (PBF-LB) is primarily governed by the dynamic regulation of melt pool behavior, which is modulated by energy density (E) [21]. Melt pool stability, which exhibits a high sensitivity to energy input, plays a critical role in dominating defect formation mechanisms. Particularly in keyhole mode (typically at $E > 50$ J/mm^3), evaporation-induced recoil pressure can destabilize the melt pool, thereby promoting pore formation [22]. Experimental results demonstrate a nonlinear relationship between energy density and relative density. As energy density increases from 21.21 J/mm^3 to 54.5 J/mm^3, the relative density improves nonlinearly from 96.852% to 99.197%, thereby confirming the existence of a critical energy density threshold (approximately 35 J/mm^3) required for adequate inter-layer bonding. Fig. 5 illustrates that at a fixed scan speed (V = 1400 mm/s), relative density initially increases and then decreases with increasing laser power (P), peaking at P = 310 W (density = 99.197%). Fig. 6 further illustrates that when P = 310 W, the maximum density is attained at V = 1400 mm/s, validating the synergistic match between power and speed for optimal energy coupling.

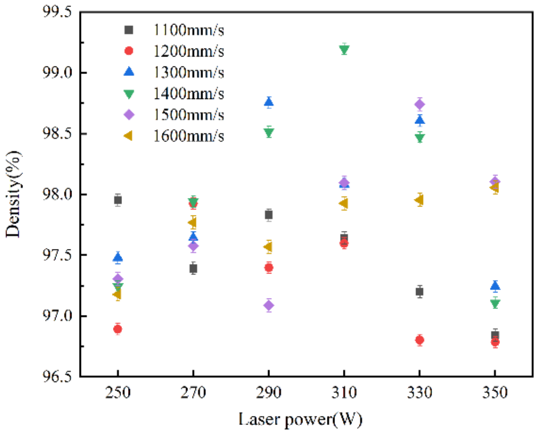

Fig. 5. Plot of laser power P versus densities

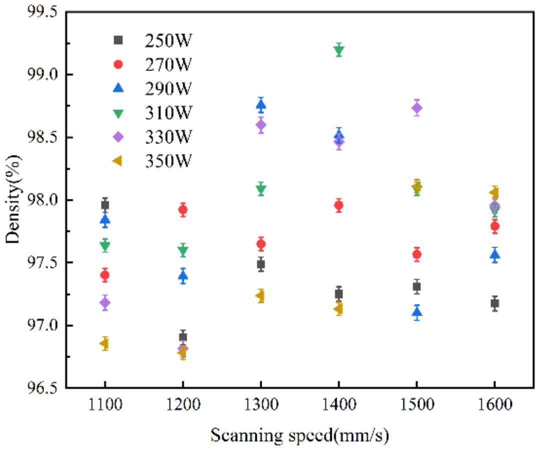

Fig. 6. Plot of scanning speed V versus densification

In the low-energy regime (E < 35 J/mm^3), discontinuous melt pools result in unmelted defects, thereby reducing density below 98.5%. Within the optimized energy range (35-42 J/mm^3), stabilized melt pools (aspect ratio ≈ 0.8) effectively suppress pore formation. At E > 45 J/mm^3, melt turbulence induces the resurgence of gas pores, resulting in a significant decline in density. Parameter sensitivity analysis reveals that scan speed (V) exerts a dominant effect on density relative to laser power (P) and layer thickness (h), while P-h interactions exacerbate pore heterogeneity. Fig. 7 demonstrates that a hatch spacing of d = 0.11 mm (overlap ratio ≈30%) results in the highest density (99.1%). Deviations (d > 0.12 mm or d < 0.10 mm) reduce density by more than 2.5%, primarily due to lack-of-fusion or remelting defects.

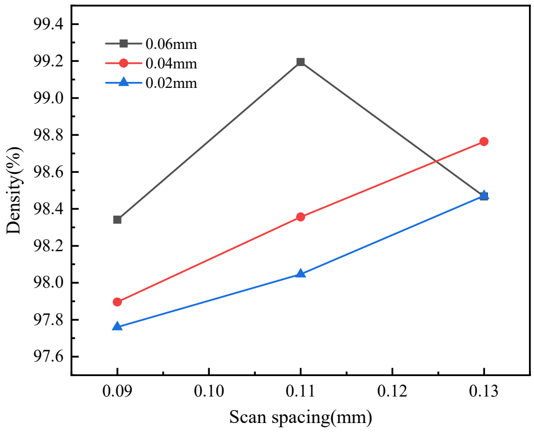

Fig. 7. Plot of scanning spacing d versus densification

The recommended process window includes: P = 300-350 W, V = 800-1200 mm/s, and h = 30-50 μm (V < 800 mm/s), supplemented by 67° interlayer rotation [23], which reduces anisotropic residual stress by 30% compared to unidirectional scanning [24], along with 200°C substrate preheating to mitigate keyhole instability. This strategy establishes a robust framework for the high-density PBF-LB fabrication of TC11 alloy components.

4. Conclusions

This study proposes a cost-effective process optimization framework for laser powder bed fusion (PBF-LB) of TC11 titanium alloy impellers, facilitating the synergistic control of both deformation and densification. The key findings are summarized as follows:

Through finite element simulations and 3D laser scanning experiments, a quantitative relationship between energy density ($E = P/(V\cdot d\cdot h)$) and residual deformation was established, with the maximum predicted deviation not exceeding 0.08 mm. At identical energy densities, deformation variations resulting from fluctuations in a single parameter remained below 3%, demonstrating that energy density serves as a robust and unified indicator for deformation control.

Laser power and scanning speed exert a significant influence on densification. Based on the empirical formula for melt pool stability regulation, $P = 0.2V + 30$, a relative density of 99.2% was achieved at P = 310 W and V = 1400 mm/s, reducing process debugging efforts by 60% compared to traditional trial-and-error methods.

Within the energy density range of 35-42 J/mm^3, relative densities exceeding 99.0% and deformations below 0.15 mm were attained, establishing a viable process window for the direct fabrication of precision components, such as aviation engine combustion chamber liners.

Acknowledgements

This research was supported by the 2024 University Industry Support Project of Gansu Province (Grant No. 2024CYZC-20).

REFERENCES

[1] S.Y. Liu, Y.C.Shin, Additive manufacturing of Ti6Al4V alloy: A review. Materials & Design **164**, 107552 (2019). DOI: https://doi.org/10.1016/j.matdes.2018.107552

[2] A.K. Singla, et al., Selective laser melting of Ti6Al4V alloy: Process parameters, defects and post-treatments. Journal of Manufacturing Processes **64**, 161-187 (2021). DOI: https://doi.org/10.1016/j.jmapro.2021.04.048

[3] E.M. Sefene, State-of-the-art of selective laser melting process. Journal of Manufacturing Systems **63**, 250-274 (2022). DOI: https://doi.org/10.1016/j.jmsy.2022.03.009

[4] A. Khorasani, et al., Effects of SLM parameters on Ti-6Al-4V properties. Additive Manufacturing **25**, 176-186 (2019). DOI: https://doi.org/10.1016/j.addma.2018.11.012

[5] H. Ali, H. Ghadbeigi, K. Mumtaz, Scan path optimization for residual stress mitigation in selective laser melting. The International Journal of Advanced Manufacturing Technology **103** (5-8), 2345-2356 (2019). DOI: https://doi.org/10.1007/s00170-019-03530-7

[6] M. Malý, P. Hořejší, A. Školáková, M. Novak, D. Vojtěch, P. Salvetr, The effect of process parameters on the relative density and deformation of 316L stainless steel produced by selective laser melting. Materials Today: Proceedings **7**, 769-775 (2019). DOI: https://doi.org/10.1016/j.matpr.2018.12.069

[7] T. Kurzynowski, K. Gruber, W. Stopyra, B. Kuźnicka, E. Chlebus, Correlation between process parameters, microstructure and properties of 316 L stainless steel processed by selective laser melting. Materials Science and Engineering A **718**, 64-73 (2018). DOI: https://doi.org/10.1016/j.msea.2018.01.103

[8] J.A. Slotwinski, E.J. Garboczi, P.E. Stutzman, C.F. Ferraris, S.S. Watson, M.A. Peltz, Characterization of metal powders used for additive manufacturing. Journal of Research of the National Institute of Standards and Technology **119**, 460-493 (2014). DOI: https://doi.org/10.6028/jres.119.018

[9] P. Hanzl, et al., Influence of SLM parameters on mechanical properties. Procedia Engineering **100**, 1405-1413 (2015). DOI: https://doi.org/10.1016/j.proeng.2015.01.516

[10] X. Li, Y. Wang, Z. Zhang, Multi-Objective Optimization of SLM Process Parameters for Ti-6Al-4V Alloy Using Orthogonal Experimental Design. Materials & Design **192**, 108714 (2020). DOI: https://doi.org/10.1016/j.matdes.2020.108714

[11] G. Miranda, et al., Thin-walled Ti6Al4V parts by SLM. Journal of Manufacturing Processes **39**, 346-355 (2019). DOI: https://doi.org/10.1016/j.jmapro.2019.02.022

[12] H. Tang ,S. Qian, L. Zhao, Response Surface Methodology-Based Optimization of Laser Powder Bed Fusion Parameters for Ti-6Al-4V Alloy with Enhanced Mechanical Properties. Additive Manufacturing **48**, 102102 (2021). DOI: https://doi.org/10.1016/j.addma.2021.102102

[13] B. Zhang, et al.,Defect formation mechanisms in SLM. Chinese Journal of Mechanical Engineering **30** (3), 515-527 (2017). DOI: https://doi.org/10.1007/s10033-017-0101-9

[14] L. Wang, et al, Residual stress prediction in SLM AlSi10Mg. International Journal of Advanced Manufacturing Technology **97**(1-4), 1469-1480 (2018). DOI: https://doi.org/10.1007/s00170-018-1996-8

[15] G. Miranda, S. Faria, F. Bartolomeu, E. Pinto, N. Alves, N. Peixinho, K.M. Gasik, F.S. Silva, A study on the production of thin-walled Ti6Al4V parts by selective laser melting. Journal of Manufacturing Processes **39**, 346-355 (2019). DOI: https://doi.org/10.1016/j.jmapro.2019.02.022

[16] R.X. Zhao et al., On the role of volumetric energy density in the microstructure and mechanical properties of laser powder bed fusion Ti-6Al-4V alloy. Addit. Manuf. **51**, 102605 (2022). DOI: https://doi.org/10.1016/j.addma.2022.102605

[17] K.G. Prashanth, S. Scudino, T. Maity, J. Das, J. Eckert, Is the energy density a reliable parameter for materials synthesis by selective laser melting? Mater. Res. Lett. **5** (6), 386-390 (2017). DOI: https://doi.org/10.1080/21663831.2017.1299808

[18] Y. Zhang, Z. Li, P. Bai, B. Liu, High-cycle fatigue behavior of SLM Ti-6Al-4V impellers under aerospace service conditions. Additive Manufacturing **45**, 102017 (2021). DOI: https://doi.org/10.1016/j.addma.2021.102017

[19] N. Saunders, Z. Guo, X. Li, A. P. Miodownik, J.-P. Schillé, JMatPro: A Materials Property Simulation Tool for Multi-Component Alloys. Materials Science Forum **706-709**, 59-64 (2012). DOI: https://doi.org/10.4028/www.scientific.net/msf.706-709.59

[20] C. Li, J. Liu, Y. Guo, Residual stress prediction in selective laser melting: A finite element approach considering powder-scale characteristics. Materials & Design **109**, 441-449. (2016). DOI: https://doi.org/10.1016/j.matdes.2016.07.046

[21] W.E. King, A.T. Anderson, R.M. Ferencz, N.E. Hodge, C. Kamath, S. A. Khairallah, Laser powder bed fusion additive manufacturing of metals: Physics, computational, and materials challenges. Acta Materialia **108**, 19-30. (2016). DOI: https://doi.org/10.1016/j.actamat.2016.02.040

[22] B. Vrancken, L. Thijs, J.-P. Kruth, J. Van Humbeeck, Heat treatment of Ti6Al4V produced by selective laser melting: Microstructure and mechanical properties. Journal of Alloys and Compounds **541**, 177-185 (2014). DOI: https://doi.org/10.1016/j.jallcom.2012.07.022

[23] B. Zhang, Y. Li, Q. Bai, Effect of interlayer rotation on microstructure and mechanical properties of selective laser melted Ti-6Al-4V alloy. Materials & Design **160**, 1-10. (2018). DOI: https://doi.org/10.1016/j.matdes.2018.08.052

[24] H., Ali, H., Ghadbeigi, K. Mumtaz, Scan path optimization for residual stress mitigation in selective laser melting. The International Journal of Advanced Manufacturing Technology **103** (5-8), 2345-2356 (2019). DOI: https://doi.org/10.1007/s00170-019-03530-7